

Nanoscale measurement of giant saturation magnetization in α'' -Fe₁₆N₂ by electron energy-loss magnetic chiral dichroism

Xinfeng Chen^a, Soma Higashikozono^b, Keita Ito^b, Lei Jin^c, Ping-Luen Ho^a, Chu-Ping Yu^{a,d}, Nyan-Hwa Tai^d, Joachim Mayer^{c,e}, Rafal E. Dunin-Borkowski^c, Takashi Suemasu^b, Xiaoyan Zhong^{a,*}

^a National Center for Electron Microscopy in Beijing, Key Laboratory of Advanced Materials (MOE), The State Key Laboratory of New Ceramics and Fine Processing, School of Materials Science and Engineering, Tsinghua University, Beijing 100084, China

^b Institute of Applied Physics, University of Tsukuba, Tsukuba, Ibaraki 305-8573, Japan

^c Ernst Ruska-Centre for Microscopy and Spectroscopy with Electrons, Forschungszentrum Jülich GmbH, Jülich 52425, Germany

^d Department of Materials Science and Engineering, National Tsing-Hua University, Hsinchu 30013, Taiwan

^e Central Facility for Electron Microscopy, RWTH Aachen University, Aachen 52074, Germany

ARTICLE INFO

Keywords:

Electron energy-loss magnetic chiral dichroism
Rare-earth-free permanent magnetic materials
Giant saturation magnetization
 α'' -Fe₁₆N₂, high spatial resolution

ABSTRACT

Metastable α'' -Fe₁₆N₂ thin films were reported to have a giant saturation magnetization of above 2200 emu/cm³ in 1972 and have been considered as candidates for next-generation rare-earth-free permanent magnetic materials. However, their magnetic properties have not been confirmed unequivocally. As a result of the limited spatial resolution of most magnetic characterization techniques, it is challenging to measure the saturation magnetization of the α'' -Fe₁₆N₂ phase, as it is often mixed with the parent α' -Fe₈N phase in thin films. Here, we use electron energy-loss magnetic chiral dichroism (EMCD), aberration-corrected transmission electron microscopy, X-ray diffraction and macroscopic magnetic measurements to study α'' -Fe₁₆N₂ (containing ordered N atoms) and α' -Fe₈N (containing disordered N atoms). The ratio of saturation magnetization in α'' -Fe₁₆N₂ to that in α' -Fe₈N is determined to be 1.31 ± 0.10 from quantitative EMCD measurements and dynamical diffraction calculations, confirming the giant saturation magnetization of α'' -Fe₁₆N₂. Crystallographic information is also obtained about the two phases, which are mixed on the nanoscale.

1. Introduction

Permanent magnetic materials are of great importance for applications that include information technology and energy conversion. Rare-earth-free permanent magnetic materials are currently attracting particular attention due to the limited availability of rare earth elements. According to the Slater-Pauling curve and classical cruise magnetic theory [1], the magnetic material with the highest saturation magnetization (M_S) is expected to be Fe₆₅Co₃₅, with a saturation magnetic induction of 2.45 T. However, in 1972 Kim and Takahashi reported an M_S value of above 2200 emu/cm³ (equivalent to ~ 2.76 T) in α'' -Fe₁₆N₂ thin films using a torque magnetometer, a magnetic balance and a torsion pendulum magnetometer [2]. Sugita et al. measured an M_S value for α'' -Fe₁₆N₂ thin films that had been grown using molecular beam epitaxy (MBE) of 2308 emu/cm³ using a vibrating sample magnetometer (VSM) and Mössbauer spectroscopy [3]. Sun et al. further confirmed an M_S value for α'' -Fe₁₆N₂ films grown using facing target

sputtering of ~ 2200 emu/cm³ using VSM [4]. Wang et al. verified an M_S value for Fe-N thin films that had an ordering parameter of ~ 0.35 of 2133 emu/cm³ using VSM and claimed, based on X-ray magnetic circular dichroism (XMCD) measurements, that the observed giant M_S value was correlated with the formation of highly localized 3d electron states [5]. In contrast, Takahashi et al. measured an M_S value for α'' -Fe₁₆N₂ films of no more than 1776 emu/cm³ using VSM and conversion electron Mössbauer spectra, which is slightly higher than that of pure Fe [6]. Sakuma determined a value for the magnetic moment of α'' -Fe₁₆N₂ of only 1731 emu/cm³ using spin-polarized band structure calculations [7]. Li et al. measured the magnetic moment of α'' -Fe₁₆N₂ to be 1850 emu/cm³ using VSM and Mössbauer spectroscopy [8]. Accordingly, although α'' -Fe₁₆N₂ is a candidate for use as a rare-earth-free permanent magnetic material [9], there is still uncertainty about its value of M_S [10]. This uncertainty results from the difficulty of phase identification, as α'' -Fe₁₆N₂ is readily mixed with the parent α' -Fe₈N phase in thin films, in combination with the fact that the spatial

* Corresponding author.

E-mail address: xyzhong@mail.tsinghua.edu.cn (X. Zhong).

<https://doi.org/10.1016/j.ultramic.2019.02.016>

Received 28 November 2018; Received in revised form 10 February 2019; Accepted 18 February 2019

Available online 19 February 2019

0304-3991/ © 2019 Elsevier B.V. All rights reserved.

resolution of most magnetic characterization methods is not sufficient to distinguish pure $\alpha''\text{-Fe}_{16}\text{N}_2$ from the parent $\alpha'\text{-Fe}_8\text{N}$ phase on the nanometer scale.

The technique of electron energy-loss magnetic chiral dichroism (EMCD) [11] in the transmission electron microscope (TEM) offers magnetic characterization with high spatial resolution and therefore a solution to these challenges. EMCD is similar to XMCD, in that it permits the quantitative element-selective determination of spin and orbital magnetic moments in crystalline materials from spectra measured at core-loss edges [12–16]. When compared with XMCD, EMCD offers higher spatial resolution, now reaching the atomic scale, in part due to the short de Broglie wavelength and penetration of high energy electrons in the TEM [17–19]. By combining scanning TEM (STEM) with electron energy-loss spectroscopy (EELS) and energy dispersive X-ray spectroscopy [20–26], structural, compositional and bonding information can be correlated with local spin configurations measured from the very same region [27–30]. In our previous study, the influence of cation ratio and order on local magnetic coupling in ordered and disordered phases of $\text{Sr}_2\text{Fe}_{1+x}\text{Re}_{1-x}\text{O}_6$ that were mixed on the nanoscale was investigated [27]. Here, we use a similar approach to study Fe-N that contains mixed phases of $\alpha''\text{-Fe}_{16}\text{N}_2$ and $\alpha'\text{-Fe}_8\text{N}$. We record structural and magnetic information from both phases in epitaxial MBE-grown Fe-N thin films. With the help of dynamical diffraction calculations, we use the EMCD measurements to quantitatively determine the ratio of M_S in $\alpha''\text{-Fe}_{16}\text{N}_2$ to that in $\alpha'\text{-Fe}_8\text{N}$, thereby experimentally confirming the giant saturation magnetization of $\alpha''\text{-Fe}_{16}\text{N}_2$.

2. Materials and methods

Fe-N thin films were grown using MBE with accurate control over their thickness and composition [31] and sizes of 5 mm \times 5 mm. Two types of thin films were prepared: one containing mixed phases of $\alpha'\text{-Fe}_8\text{N}$ and $\alpha''\text{-Fe}_{16}\text{N}_2$ and the other containing primarily $\alpha'\text{-Fe}_8\text{N}$. For the films with mixed phases, a 3 nm thick seed layer of $\alpha\text{-Fe}$ was first grown on single crystalline MgAl_2O_4 (MAO) (001). A 100 nm thick $\alpha'\text{-Fe}_8\text{N}$ layer was then grown epitaxially, followed by a 4 nm thick Ti capping layer to prevent surface oxidation, as confirmed using X-ray photoelectron spectroscopy. N ordering (*i.e.*, a phase transformation from $\alpha'\text{-Fe}_8\text{N}$ to $\alpha''\text{-Fe}_{16}\text{N}_2$) was achieved by furnace annealing at 150 °C for 50 h. Finally, a 35 nm thick SiO_2 protection layer was deposited using radio frequency (RF) sputtering. For the $\alpha'\text{-Fe}_8\text{N}$ -dominated films, a 3 nm thick $\alpha\text{-Fe}$ and an 85 nm thick $\alpha'\text{-Fe}_8\text{N}$ layer were grown epitaxially on single crystalline MAO (001) and covered by a 4 nm thick Ti capping layer. A 35 nm thick SiO_2 protection layer was then deposited using RF sputtering.

$\alpha'\text{-Fe}_8\text{N}$ and $\alpha''\text{-Fe}_{16}\text{N}_2$ have tetragonal structures with lattice parameters of $a = b = 2.86 \text{ \AA}$, $c = 3.15 \text{ \AA}$ and $a = b = 5.72 \text{ \AA}$, $c = 6.29 \text{ \AA}$, respectively. The N atoms in blue are distributed randomly in $\alpha'\text{-Fe}_8\text{N}$, as shown in Fig. 1a. In contrast, in ordered metastable $\alpha''\text{-Fe}_{16}\text{N}_2$, N atoms in blue occupy half of the octahedral interstices [32], while Fe atoms (Fe I in red, Fe II in green and Fe III in yellow) occupy three different sites that are designated 4d, 8h and 4c, as shown in Fig. 1b. The site occupancy ratio of Fe I (4d), Fe II (8h) and Fe III (4c) is 1: 2: 1, with four Fe atoms on the 4d site, eight Fe atoms on the 8h site and four Fe atoms on the 4c site [8].

X-ray diffraction (XRD) measurements were performed using a high power IP crystal X-ray R-Axis Spider diffractometer. Magnetic hysteresis ($M\text{-}H$) loops were measured between $-15,000$ and $15,000$ Oe at room temperature (RT) using a superconducting quantum interference device (SQUID) VSM from Quantum Design. Selected area electron diffraction (SAED) patterns, low magnification and dark-field (DF) TEM images were recorded on an FEI Tecnai G² 20 TEM operated at 200 kV. High-angle annular dark-field (HAADF) STEM imaging was performed at 300 kV on an FEI Titan Cubed Themis G2 300 TEM, which is equipped with a double spherical aberration corrector and has a spatial resolution of 0.06 nm in STEM mode. EELS and EMCD spectra were

recorded under parallel beam illumination conditions at 300 kV on an FEI Titan 80–300 TEM equipped with a post column Gatan Tridiem imaging filter with an energy resolution of ~ 0.7 eV, a beam size of ~ 80 nm or less, an incident beam convergence semi-angle of ~ 0.3 mrad and a collection semi-angle of ~ 2.5 mrad. Nanodiffraction experiments were performed at 300 kV on an FEI Titan 80–300 TEM using a beam size of ~ 2 nm [33]. EELS and EMCD experiments under nanobeam illumination conditions were performed at 300 kV on an FEI Titan Cubed Themis G2 300 TEM equipped with a Gatan Quantum imaging filter with an energy resolution of ~ 1 eV, a beam size of ~ 2 nm or more and convergence and collection semi-angles of ~ 0.92 mrad and ~ 1.98 mrad, respectively. Each EMCD experiment was performed in an optimal two-beam diffraction condition (2BC) based on theoretical dynamical diffraction calculations performed using software that can realize accurate summation over Bloch waves and their plane wave components [34]. EMCD spectra were extracted from differences between pairs of normalized spectra taken at “+” and “−” Thales positions, while corresponding low-loss spectra were acquired under the same convergence and collection angles with the same detection aperture centered on the transmitted beam for estimating the sample thickness. Data processing of the spectra included pre-edge background subtraction, removal of plural scattering using Fourier ratio deconvolution and normalization by integration of the post-edge intensity.

3. Structural characterization of $\alpha'\text{-Fe}_8\text{N}$ and $\alpha''\text{-Fe}_{16}\text{N}_2$

A TEM image and a corresponding SAED pattern of an 85 nm thick film of the $\alpha'\text{-Fe}_8\text{N}$ -dominant phase on MAO are shown in Figs 1c and 1f, respectively. The SAED pattern reveals an epitaxial MAO[100] (001)//Fe[110](001)// $\alpha'\text{-Fe}_8\text{N}$ [110](001) orientation relationship, without any superlattice diffraction spots from ordered $\alpha''\text{-Fe}_{16}\text{N}_2$. A TEM image and a SAED pattern of a 100 nm thick film of the mixed phases $\alpha'\text{-Fe}_8\text{N}$ and $\alpha''\text{-Fe}_{16}\text{N}_2$ on MAO are shown in Figs 1d and 1g, respectively. The SAED pattern reveals superlattice diffraction spots originating from ordered $\alpha''\text{-Fe}_{16}\text{N}_2$ and an epitaxial MAO[100](001)// $\alpha\text{-Fe}$ [110](001)// $\alpha'\text{-Fe}_8\text{N}$ [110](001)// $\alpha''\text{-Fe}_{16}\text{N}_2$ [110](001) orientation relationship. The $(\bar{1}1\bar{2})$ of $\alpha''\text{-Fe}_{16}\text{N}_2$ superlattice diffraction spot, which is marked by a red circle, was used to form the DF image shown in Fig. 1e. In this image, nanosized $\alpha''\text{-Fe}_{16}\text{N}_2$ regions can be seen to be distributed randomly in the film.

Fig. 2a shows an HAADF STEM image of Fe-N thin films that contain mixed phases viewed along the [100] zone axis of MAO. The image reveals the atomic structures of $\alpha'\text{-Fe}_8\text{N}$, $\alpha''\text{-Fe}_{16}\text{N}_2$, the Fe seed layer and the MAO substrate, with a perfect MAO[100](001)// $\alpha\text{-Fe}$ [110] (001)// $\alpha'\text{-Fe}_8\text{N}$ [110](001)// $\alpha''\text{-Fe}_{16}\text{N}_2$ [110](001) epitaxial orientation relationship. A corresponding diffraction pattern recorded from the MAO substrate is shown as an inset. Regions of $\alpha''\text{-Fe}_{16}\text{N}_2$, which are marked by white dashed boxes, are contained within the parent $\alpha'\text{-Fe}_8\text{N}$ phase. Figs. 2b and c show magnified HAADF STEM images of $\alpha'\text{-Fe}_8\text{N}$ and $\alpha''\text{-Fe}_{16}\text{N}_2$, respectively. The atomic number (Z) contrast of each column in $\alpha'\text{-Fe}_8\text{N}$ is almost identical, since the N atoms are distributed randomly. In comparison, there is a modulation of the Z contrast of the columns in $\alpha''\text{-Fe}_{16}\text{N}_2$ due to the ordered arrangement of N atoms. The appearance of superlattice diffraction spots originating from ordered $\alpha''\text{-Fe}_{16}\text{N}_2$ is visible in the nanodiffraction patterns shown as an inset to Fig. 2c, while there are no superlattice spots in corresponding nanodiffraction patterns of $\alpha'\text{-Fe}_8\text{N}$ shown as an inset to Fig. 2b. Supplementary Figs. S1a and S1b show EEL spectra recorded from $\alpha'\text{-Fe}_8\text{N}$ -dominant and mixed phase films, respectively. The spectra confirm the absence of significant oxidation of both samples, as there is no detectable O K edge.

Figs. 3a and b show raw XRD patterns recorded from the $\alpha'\text{-Fe}_8\text{N}$ -dominant and mixed phase films, respectively. The degree of N site ordering, D , can be determined from the integrated intensity ratio of the $I(002)$ and $I(004)$ peaks after background subtraction and peak identification by using the expression [5]

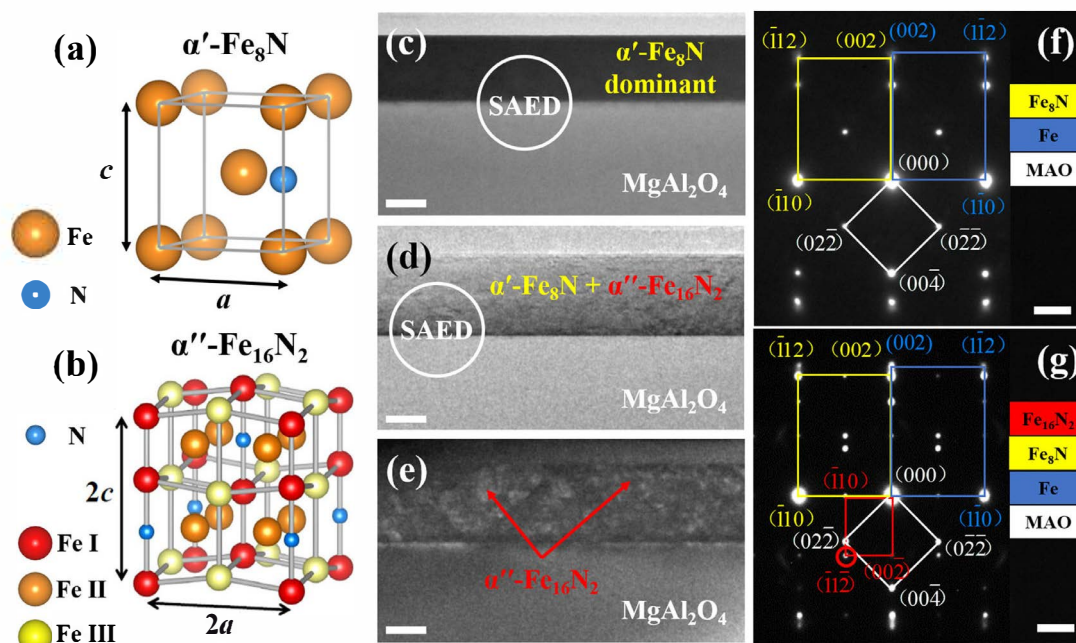


Fig. 1. (a) Crystallographic structure of α' - Fe_8N with randomly distributed N atoms (in blue, while Fe in brown). (b) Crystallographic structure of α'' - Fe_{16}N_2 with ordered N atoms (in blue) occupying half of the octahedral interstices and three Fe atoms (Fe I in red, Fe II in brown and Fe III in yellow) occupying different sites, which are designated 4d, 8h and 4c. (c) TEM image and (f) corresponding SAED pattern of an 85 nm thick film of the α' - Fe_8N -dominant phase on a MgAl_2O_4 (MAO) substrate (where MAO in white, α -Fe in blue and α' - Fe_8N in yellow). The SAED pattern reveals an epitaxial MAO[100](001)// α -Fe[110](001)// α' - Fe_8N [110](001) orientation relationship without any superlattice diffraction spots of ordered α'' - Fe_{16}N_2 . (d) TEM image and (g) corresponding SAED pattern of a 100 nm thick film of mixed α' - Fe_8N and α'' - Fe_{16}N_2 on MAO. The SAED pattern reveals superlattice spots of ordered α'' - Fe_{16}N_2 (where MAO in white, α -Fe in blue, α' - Fe_8N in yellow and α'' - Fe_{16}N_2 in red) and an epitaxial MAO[100](001)// α -Fe[110](001)// α' - Fe_8N [110](001)// α'' - Fe_{16}N_2 [110](001) orientation relationship. The $(1\bar{1}\bar{2})$ α'' - Fe_{16}N_2 superlattice spot marked by a red circle in (g) was used to form the dark-field TEM image shown in (e), which reveals nanosized α'' - Fe_{16}N_2 regions distributed randomly in the film. The scale bars in (c), (d) and (e) are 50 nm, while those in (f) and (g) are 2 1/nm. (For interpretation of the references to colour in this figure legend, the reader is referred to the web version of this article.)

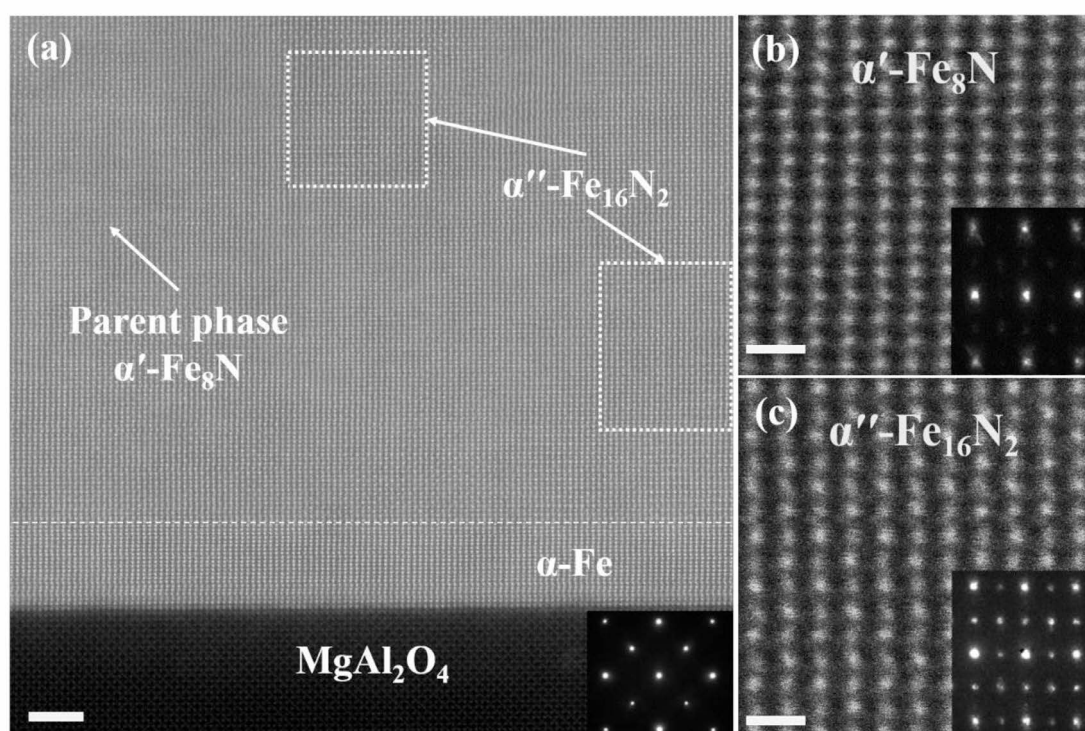


Fig. 2. (a) HAADF STEM image of interfaces between the MgAl_2O_4 (MAO) substrate and the Fe-N thin films with mixed phases of α' - Fe_8N , α'' - Fe_{16}N_2 and an Fe seed layer, revealing a perfect epitaxial MAO[100](001)// α -Fe[110](001)// α' - Fe_8N [110](001)// α'' - Fe_{16}N_2 [110](001) orientation relationship. A corresponding diffraction pattern from MAO is shown in the inset. Representative α'' - Fe_{16}N_2 regions, which are marked by white dashed boxes, are contained within the parent α' - Fe_8N phase. (b) and (c) show HAADF STEM images and corresponding nanodiffraction patterns recorded from α' - Fe_8N and α'' - Fe_{16}N_2 , respectively. Superlattice diffraction spots are visible from ordered α'' - Fe_{16}N_2 , but not from α' - Fe_8N . The scale bars are 2 nm in (a) and 0.5 nm in (b) and (c).

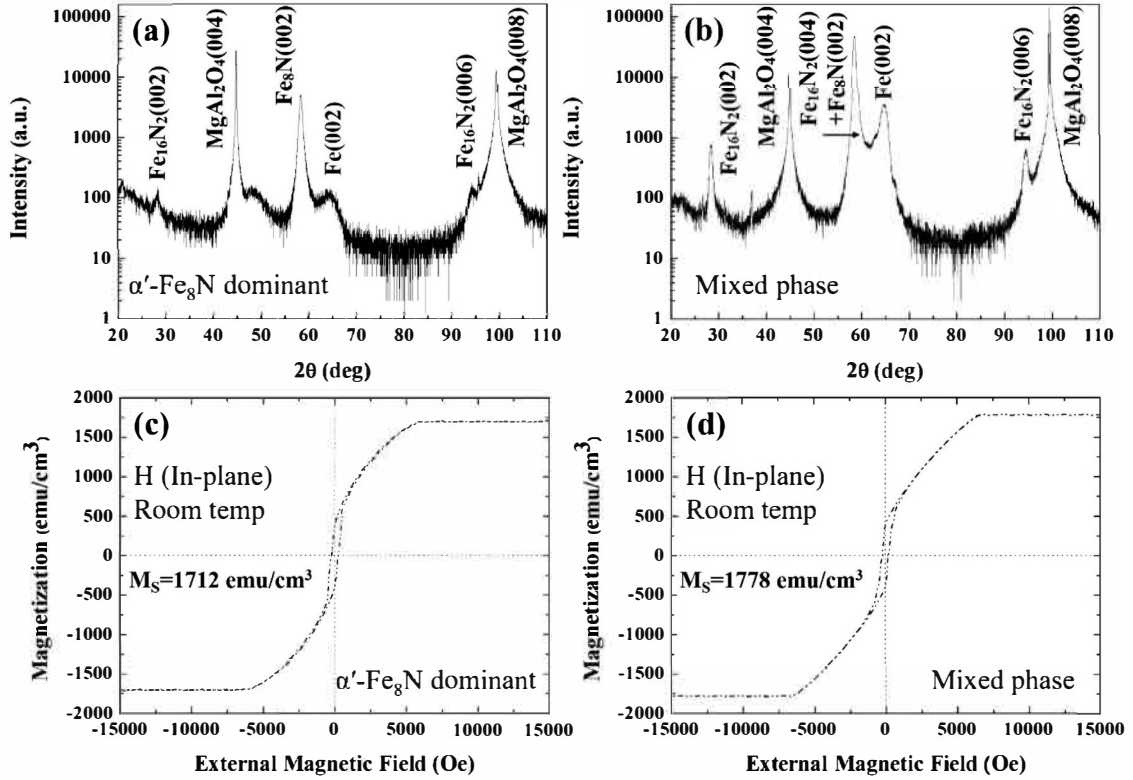


Fig. 3. (a, b) Raw X-ray diffraction patterns recorded from (a) the α' -Fe₈N-dominant and (b) the mixed phase films, respectively. (c, d) Magnetic hysteresis (M - H) loops recorded from (c) the α' -Fe₈N-dominant and (d) the mixed phase films, respectively, during the application of an in-plane magnetic field parallel to their surfaces at room temperature.

$$D = \frac{I^{obs}(002)/I^{obs}(004)}{I^{cal}(002)/I^{cal}(004)}, \quad (1)$$

where $I^{obs}(002)$ and $I^{obs}(004)$ are the integrated intensities of the α' -Fe₁₆N₂ (002) and (004) peaks, respectively. It is worth noting that $I^{obs}(004)$ for α' -Fe₁₆N₂ contains contributions from both α' -Fe₁₆N₂ (004) and α' -Fe₈N (002). Based on structure factor calculations for fully ordered single crystalline α' -Fe₁₆N₂, $I^{cal}(002)$ and $I^{cal}(004)$ represent the integrated intensities of α' -Fe₁₆N₂ (002) and (004), respectively, while the ratio of $I^{cal}(002)/I^{cal}(004)$ is 0.125 [3]. Using Eq. (1), the degree of N site ordering is determined to be 0.61% and 10.15% in the α' -Fe₈N-dominant and mixed phase thin films, respectively.

4. Magnetic characterization of α' -Fe₈N and α' -Fe₁₆N₂

4.1. Saturation magnetization determination by macroscopic measurements

Figs. 3c and d show M - H loops recorded from the α' -Fe₈N-dominant and mixed phase films, respectively, during the application an in-plane magnetic field parallel to their surfaces at RT. Contributions from the 3 nm thick α -Fe seed layer were removed from the measured saturation magnetization for both samples. Assuming that the contribution of α' -Fe₁₆N₂ is negligible in the α' -Fe₈N-dominant films, in which the degree of N site ordering is 0.61%, the M_S value of α' -Fe₈N is inferred to be 1712 emu/cm³, in good agreement with previous reports [5, 35]. In contrast, the M_S value of the mixed phase thin films was measured to be 1778 emu/cm³. Although M_S can be seen to increase with the degree of N site ordering, we can only approximately estimate the M_S value of α' -Fe₁₆N₂ as 2362 emu/cm³ based on the value of 10.15% α' -Fe₁₆N₂ in the sample, since the spatial resolution of the macroscopic magnetic measurement is not sufficient to distinguish the α' -Fe₁₆N₂ phase from the parent α' -Fe₈N phase in the mixed phase thin films.

4.2. Saturation magnetization determination by nanoscale EMCD measurements

According to sum rules [15,16], the total magnetic moment $\langle\mu\rangle$ can be determined from experimental EEL spectra S_+ and S_- recorded at positions “+” and “-”, respectively (as shown in Fig. 4), taking into account the dynamical diffraction coefficients K . Assuming that the magnetic dipole term T_z is negligible in the pseudo-cubic Fe-N system:

$$\begin{aligned} \langle\mu\rangle &= -\mu_B(\langle L\rangle + 2\langle S\rangle) \\ &= -\mu_B \left[\left(\frac{2N_h}{K} \right) \frac{\int_{L_3+L_2} (S_+ - S_-) dE}{\int_{L_3+L_2} (S_+ + S_-) dE} \right. \\ &\quad \left. + \left(\frac{3N_h}{K} \right) \frac{\int_{L_3} (S_+ - S_-) dE - 2 \int_{L_2} (S_+ - S_-) dE}{\int_{L_3+L_2} (S_+ + S_-) dE} \right] \\ &= -\mu_B \frac{N_h}{K} \left[\frac{5 \int_{L_3} (S_+ - S_-) dE - 4 \int_{L_2} (S_+ - S_-) dE}{\int_{L_3+L_2} (S_+ + S_-) dE} \right] \end{aligned} \quad (2)$$

where N_h is the number of holes, μ_B is the Bohr magneton and $\langle S\rangle$ and $\langle L\rangle$ are the ground state expectation values of spin and orbital momentum, respectively. The values of N_h for α' -Fe₈N and α' -Fe₁₆N₂ are equal because they have the same chemical valence. The ratio between the total magnetic moment of α' -Fe₈N and α' -Fe₁₆N₂, which represents the ratio between the M_S values of α' -Fe₈N and α' -Fe₁₆N₂, can be written in the form

$$\frac{\langle\mu\rangle_{\alpha'-Fe_{16}N_2}}{\langle\mu\rangle_{\alpha'-Fe_8N}} = \frac{\left[\frac{5 \int_{L_3} (S_+ - S_-) dE - 4 \int_{L_2} (S_+ - S_-) dE}{\int_{L_3+L_2} (S_+ + S_-) dE} \right]_{\alpha'-Fe_{16}N_2}}{\left[\frac{5 \int_{L_3} (S_+ - S_-) dE - 4 \int_{L_2} (S_+ - S_-) dE}{\int_{L_3+L_2} (S_+ + S_-) dE} \right]_{\alpha'-Fe_8N}} \frac{K_{\alpha'-Fe_8N}}{K_{\alpha'-Fe_{16}N_2}} \quad (3)$$

Since the M_S value of α' -Fe₈N has been determined accurately in

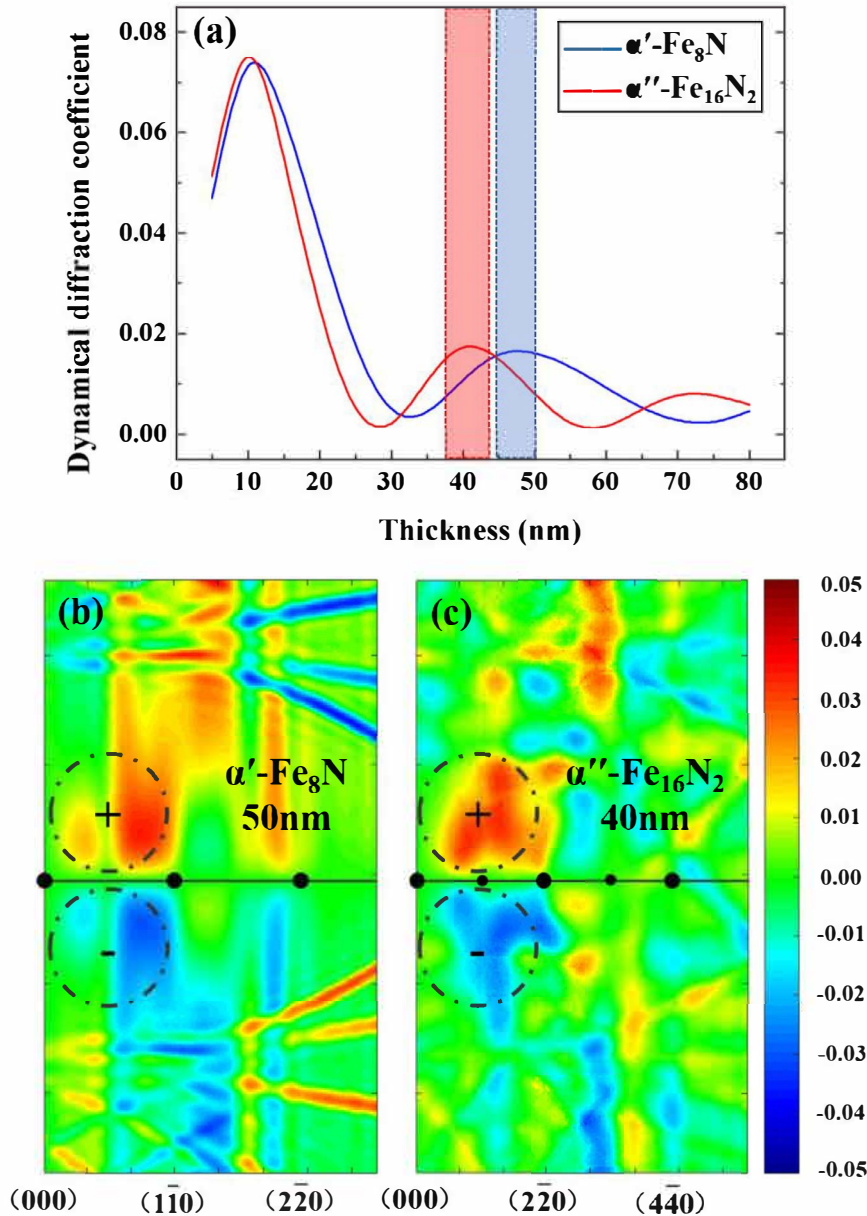


Fig. 4. (a) Calculated thickness-dependent dynamical diffraction coefficients for α' -Fe₈N (in blue) and α'' -Fe₁₆N₂ (in red), the relevant optimal thickness window for EMCD experiment is shadowed by blue and red, respectively. The calculations were performed for α' -Fe₈N in a two beam condition with (110) systematic reflections excited and for α'' -Fe₁₆N₂ in a two beam condition with (220) systematic reflections excited. Distributions of relative dynamical diffraction coefficients for (b) 50-nm-thick α' -Fe₈N and (c) 40-nm-thick α'' -Fe₁₆N₂. Optimal positive and negative positions of the detection aperture in the Thales circle in the diffraction plane are marked “+” and “-”, respectively. (For interpretation of the references to colour in this figure legend, the reader is referred to the web version of this article.)

previous studies [5, 35], the ratio $\langle \mu \rangle_{\alpha''\text{-Fe}_{16}\text{N}_2} / \langle \mu \rangle_{\alpha'\text{-Fe}_8\text{N}}$ can be used to infer M_S for α'' -Fe₁₆N₂.

In order to calculate the coefficients K , dynamical diffraction calculations were performed for a 2BC for α' -Fe₈N with (110) systematic reflections excited and for a 2BC for α'' -Fe₁₆N₂ with (220) systematic reflections excited. Fig. 4a shows the resulting thickness-dependent dynamical diffraction coefficients for α' -Fe₈N and α'' -Fe₁₆N₂ obtained from K values averaged within the Thales circles that are marked “+” and “-” in Figs 4b and 4c, respectively. Although the maximum value of K was achieved in α' -Fe₈N and α'' -Fe₁₆N₂ for a thickness of ~ 11 nm, it was found to be too sensitive to thickness variations between 5 and 20 nm. At the second maximum value, close to which the K value is not that sensitive to thickness variations, the optimized thickness regions for α' -Fe₈N and α'' -Fe₁₆N₂ were selected to be 45–50 nm and 38–44 nm, marked by red and blue frame in Fig. 4a, respectively.

Figs. 4b and c show representative calculated distributions of dynamical diffraction coefficients at 50-nm-thick α' -Fe₈N and 40-nm-thick α'' -Fe₁₆N₂, respectively. Optimal “+” and “-” positions for the detection aperture are marked.

With the aid of the theoretical dynamical diffraction calculations, EMCD experiments were performed from a 49 nm thick α' -Fe₈N phase in a 2BC with (110) systematic reflections excited, as shown in the inset to Fig. 5a, while EMCD experiments were performed from a 43 nm thick α'' -Fe₁₆N₂ phase in a 2BC with (220) systematic reflections excited, revealing the expected superlattice diffraction spots for α'' -Fe₁₆N₂, as shown in the inset to Fig. 5b. The K values for 49-nm-thick α' -Fe₈N and 43-nm-thick α'' -Fe₁₆N₂, averaged across the optimized aperture positions, are almost equivalent. Under these circumstances:

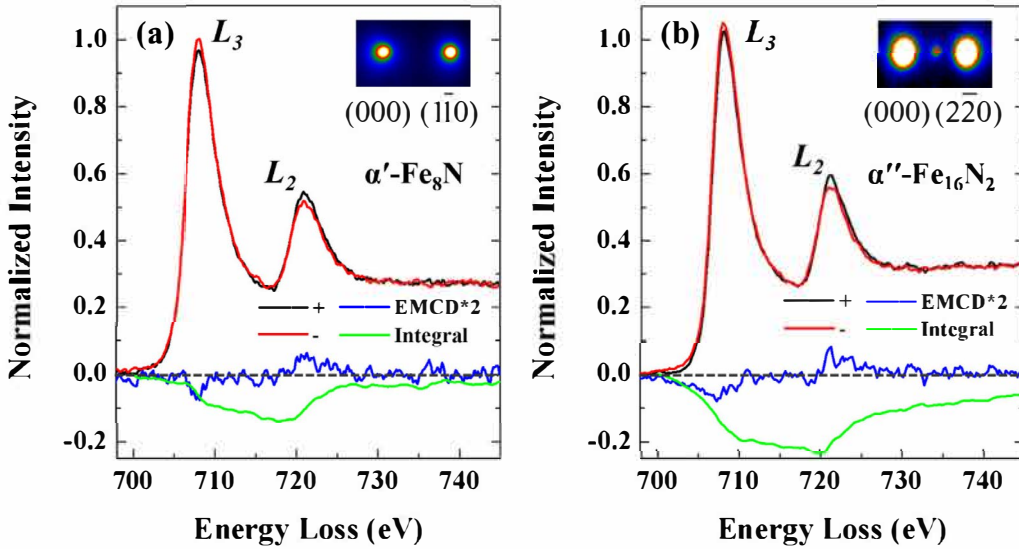


Fig. 5. EMCD spectra (in blue), their integrals (in green) and EEL spectra recorded at “+” (black) and “-” (red) positions for (a) α' -Fe₈N and (b) α'' -Fe₁₆N₂ after normalization by the isotropic spectra. Corresponding diffraction patterns for a two beam condition are shown as insets. (For interpretation of the references to colour in this figure legend, the reader is referred to the web version of this article.)

$$\frac{K_{\alpha'-\text{Fe}_8\text{N}}}{K_{\alpha''-\text{Fe}_{16}\text{N}_2}} = 0.98 \quad (4)$$

Supplementary Figs S2a and S2b show representative low-loss EEL spectra recorded from the α' -Fe₈N-dominant and mixed phase films, respectively, including thickness information about the experimental areas. The magnetic field of the objective lens in the TEM was perpendicular to the plane of the cross-sectional TEM sample, which is equivalent to applying an external magnetic field to the Fe-N thin films in an in-plane direction. During the experiments, the Fe-N TEM samples were saturated magnetically in both TEM and STEM mode in a magnetic field of approximately 2 T, which is much larger than the saturation in-plane magnetic field of ~ 0.65 T, according to the macroscopic M - H loops shown in Figs 3c and d. Magnetic moments calculated from the measured EMCD spectra therefore correspond to the saturation magnetization of each material. Figs. 5a and b show normalized EMCD spectra plotted in blue and EEL spectra recorded at “+” (black) and “-” (red) positions for α' -Fe₈N and α'' -Fe₁₆N₂, respectively. According to Eq. (3), in order to compare the saturation magnetizations of α' -Fe₈N and α'' -Fe₁₆N₂ quantitatively, the EMCD spectra ($S_+ - S_-$) were normalized by the intensities of the corresponding isotropic spectra $\int_{L_3+L_2} (S_+ + S_-)dE$, which were calculated by subtracting step functions from integrals of the $L_{3,2}$ edges of EEL spectra acquired at the “+” and “-” positions [36]. The details of the procedure are described in the Supplementary Fig. S3 and the related section. By making use of Eq. (4), Eq. (3) can be rewritten in the form

$$\frac{\langle \mu \rangle_{\alpha''-\text{Fe}_{16}\text{N}_2}}{\langle \mu \rangle_{\alpha'-\text{Fe}_8\text{N}}} = \frac{[5 \int_{L_3} (S_{N+} - S_{N-})dE - 4 \int_{L_2} (S_{N+} - S_{N-})dE]_{\alpha''-\text{Fe}_{16}\text{N}_2}}{[5 \int_{L_3} (S_{N+} - S_{N-})dE - 4 \int_{L_2} (S_{N+} - S_{N-})dE]_{\alpha'-\text{Fe}_8\text{N}}} \times 0.98 \quad (5)$$

where S_{N+} and S_{N-} refer to the EEL spectra S_+ and S_- after normalization by the isotropic spectra $\int_{L_3+L_2} (S_+ + S_-)dE$.

The ratio of the M_S value of α' -Fe₈N to that of α'' -Fe₁₆N₂ was determined from the intensities of the L_3 edge (from 704 to 717.2 eV) and the L_2 edge (from 717.2 to 728 eV) in the normalized EMCD spectra ($S_{N+} - S_{N-}$) for both α' -Fe₈N and α'' -Fe₁₆N₂ in the form

$$\frac{M_{S(\alpha''-\text{Fe}_{16}\text{N}_2)}}{M_{S(\alpha'-\text{Fe}_8\text{N})}} = \frac{\langle \mu \rangle_{\alpha''-\text{Fe}_{16}\text{N}_2}}{\langle \mu \rangle_{\alpha'-\text{Fe}_8\text{N}}} = 1.31 \pm 0.10 \quad (6)$$

According to the sum rules [15, 16], the orbital to spin magnetic moment ratios (m_L/m_S) obtained from the EMCD spectra for α' -Fe₈N and α'' -Fe₁₆N₂ are 0.04 ± 0.01 and 0.09 ± 0.03 , respectively.

Errors were estimated from the standard deviations of individual

experimental measurements, noise in the spectra, standard deviations of the sample thickness measurements and uncertainty in the dynamical diffraction coefficient K , following the method of error analysis presented in our previous work [13].

The M_S value of α' -Fe₈N measured using SQUID-VSM, as shown in Fig. 3c, is 1712 emu/cm^3 , which is similar to results reported previously [5,35]. The M_S value of α'' -Fe₁₆N₂ is therefore inferred to be given by the expression

$$M_{S(\alpha''-\text{Fe}_{16}\text{N}_2)} = 1.31 \times M_{S(\alpha'-\text{Fe}_8\text{N})} = 1.31 \times 1712 \text{ emu/cm}^3 = 2243 \text{ emu/cm}^3 \quad (7)$$

which is close to the value of 2250 emu/cm^3 reported in 1972 [2] and consistent with the value of 2362 emu/cm^3 estimated from XRD and SQUID measurements in this paper. Giant magnetism in α'' -Fe₁₆N₂ is therefore confirmed using EMCD.

5. Conclusion

Local structural and magnetic information about nanoscale phases of α' -Fe₈N and α'' -Fe₁₆N₂ in Fe-N thin films has been obtained experimentally using EMCD and analytical high-resolution TEM. Disordered α' -Fe₈N and ordered α'' -Fe₁₆N₂ phases have been distinguished from each other using nanodiffraction patterns and HAADF STEM imaging. Quantitative EMCD and dynamical diffraction calculations have been used to demonstrate that the M_S value of α'' -Fe₁₆N₂ is 1.31 times that of α' -Fe₈N. Based on the M_S value for α' -Fe₈N determined using macroscopic SQUID-VSM measurements, the M_S value for α'' -Fe₁₆N₂ is estimated to be 2243 emu/cm^3 , thereby experimentally confirming giant magnetism in α'' -Fe₁₆N₂. Our approach provides important insight into structure-property relationships in α' -Fe₈N and α'' -Fe₁₆N₂ phases in Fe-N thin films on the nm scale. The same approach can be applied in future studies of other nanoscale magnetic materials.

Acknowledgments

The work was supported financially by the National Key Research and Development Program [2016YFB0700402], National Natural Science Foundation of China [11834009, 51761135131, 51822105, 51671112, 51788104] National Basic Research Program of China [2015CB921700], Fund of Key Laboratory of Advanced Materials of Ministry of Education [2018AML12] and the RWTH Aachen University - Tsinghua University Junior Research Fellowship scheme. R.D.-B. is grateful for funding from the European Research Council under the

European Union's Seventh Framework Program [FP7/2007-2013]/ERC grant agreement number 320832. This work made use of the resources of the National Center for Electron Microscopy in Beijing and the Ernst Ruska-Centre for Microscopy and Spectroscopy with Electrons in Forschungszentrum Jülich. The authors thank Prof. J. Zhu, Prof. J.-P. Wang and Dr. Q. Q. Lan for valuable discussions and contributions to this work.

Supplementary materials

Supplementary material associated with this article can be found, in the online version, at doi:10.1016/j.ultramic.2019.02.016.

References

- [1] J.C. Slater, Electronic structure of alloys, *J. Appl. Phys.* 8 (1937) 385–390.
- [2] T.K. Kim, M. Takahashi, New magnetic material having ultrahigh magnetic moment, *Appl. Phys. Lett.* 20 (1972) 494–494.
- [3] Y. Sugita, H. Takahashi, M. Komuro, K. Mitsuoka, A. Sakuma, Magnetic and Mössbauer studies of single-crystal Fe_{16}N_2 and Fe-N martensite films epitaxially grown by molecular beam epitaxy (invited), *J. Appl. Phys.* 76 (1994) 6637–6641.
- [4] D.C. Sun, E.Y. Jiang, M.B. Tian, C. Lin, X.X. Zhang, Epitaxial single crystal Fe_{16}N_2 films grown by facing targets sputtering, *J. Appl. Phys.* 79 (1996) 5440–5442.
- [5] J.P. Wang, N. Ji, X.Q. Liu, Y.H. Xu, C. Sánchez-Hanke, Y.M. Wu, F.M.F. de Groot, L.F. Allard, E. Lara-Curzio, Fabrication of Fe_{16}N_2 films by sputtering process and experimental investigation of origin of giant saturation magnetization in Fe_{16}N_2 , *IEEE Trans. Magn.* 48 (2012) 1710–1717.
- [6] M. Takahashi, H. Shoji, H. Takahashi, H. Nashi, T. Wakiyama, M. Doi, M. Matsui, Magnetic moment of α' - Fe_{16}N_2 films (invited), *J. Appl. Phys.* 76 (1994) 6642–6647.
- [7] A. Sakuma, Electronic and magnetic structure of iron nitride, Fe_{16}N_2 (invited), *J. Appl. Phys.* 79 (1996) 5570–5575.
- [8] Z.W. Li, A.H. Morrish, C. Ortiz, Mössbauer studies of α' - Fe_{16}N_2 and α' - Fe_8N films, *J. Mater. Sci.* 36 (2001) 5835–5838.
- [9] Y.F. Jiang, M.A. Mehedi, E.G. Fu, Y.Q. Wang, J.-P. Wang, FeN foils by nitrogen ion-implantation, *J. Appl. Phys.* 115 (2014) 17A753.
- [10] M. Takahashi, H. Shoji, α' -FeN problem-giant magnetic moment or not, *J. Magn. Mater.* 208 (2000) 145–157.
- [11] P. Schattschneider, S. Rubino, C. Hébert, J. Ruzs, J. Kuneš, P. Novák, E. Carlino, M. Fabrizio, G. Panaccione, G. Rossi, Detection of magnetic circular dichroism using a transmission electron microscope, *Nature* 441 (2006) 486–488.
- [12] H. Lidbaum, J. Ruzs, A. Liebig, B. Hjörvarsson, P.M. Oppeneer, E. Coronel, O. Eriksson, K. Leifer, Quantitative magnetic information from reciprocal space maps in transmission electron microscopy, *Phys. Rev. Lett.* 102 (2009) 037201.
- [13] Z.Q. Wang, X.Y. Zhong, R. Yu, Z.Y. Cheng, J. Zhu, Quantitative experimental determination of site-specific magnetic structures by transmitted electrons, *Nat. Commun.* 4 (2013) 1395.
- [14] D.S. Song, G. Li, J.W. Cai, J. Zhu, A general way for quantitative magnetic measurement by transmitted electrons, *Sci. Rep.* 6 (2016) 18489.
- [15] J. Ruzs, O. Eriksson, P. Novák, P.M. Oppeneer, Sum rules for electron energy loss near edge spectra, *Phys. Rev. B* 76 (2007) 060408.
- [16] L. Calmels, F. Houdellier, B. Warot-Fonrose, C. Gatel, M.J. Hÿtch, V. Serin, E. Snoeck, P. Schattschneider, Experimental application of sum rules for electron energy loss magnetic chiral dichroism, *Phys. Rev. B* 76 (2007) 060409.
- [17] Z.C. Wang, A.H. Tavabi, L. Jin, J. Ruzs, D. Tyutyunnikov, H.B. Jiang, Y. Moritomo, J. Mayer, R.E. Dunin-Borkowski, R. Yu, J. Zhu, X.Y. Zhong, Atomic scale imaging of magnetic circular dichroism by achromatic electron microscopy, *Nat. Mater.* 17 (2018) 221–225.
- [18] J. Ruzs, S. Muto, J. Spiegelberg, R. Adam, K. Tatsumi, D.E. Bürgler, P.M. Oppeneer, C.M. Schneider, Magnetic measurements with atomic-plane resolution, *Nat. Commun.* 7 (2016) 12672.
- [19] T. Thersleff, J. Ruzs, B. Hjörvarsson, K. Leifer, Detection of magnetic circular dichroism with subnanometer convergent electron beams, *Phys. Rev. B* 94 (2016) 134430.
- [20] D.A. Muller, Structure and bonding at the atomic scale by scanning transmission electron microscopy, *Nat. Mater.* 8 (2009) 263–270.
- [21] X.Y. Zhong, J. Zhu, A.H. Zhang, H-2-induced environmental embrittlement in ordered and disordered Ni_3Fe : an electronic structure approach, *Intermetallics* 15 (2007) 495–499.
- [22] Y.C. Chen, X.Y. Zhong, B. Kabius, J.M. Hiller, N.-H. Tai, I.N. Lin, Improvement of field emission performance on nitrogen ion implanted ultrananocrystalline diamond films through visualization of structure modifications, *Diam. Relat. Mater.* 20 (2011) 238–241.
- [23] X.Y. Zhong, J. Zhu, J.Y. Liu, Study of the interfacial structure of a Pt/a- Al_2O_3 model catalyst under high temperature hydrogen reduction, *J. Catal.* 236 (2005) 9–13.
- [24] Z. Lin, J. Z. Han, J.B. Yang, X.P. Kong, X.Y. Zhong, S.Q. Liu, X.D. Zhang, C.S. Wang, H.L. Du, Y.C. Yang, Self-organized rod-like nanostructure in $\text{Pr}_2\text{Fe}_{14}\text{B}$ -type alloy and its role in inducing texture during the early stages of disproportionation, *Phys. Rev. B* 83 (2011) 206–209.
- [25] X.Y. Zhong, B. Kabius, D.K. Schreiber, J.A. Eastman, D.D. Fong, A.K. Petford-Long, Three-dimensional quantitative chemical roughness of buried $\text{ZrO}_2/\text{In}_2\text{O}_3$ interfaces via energy-filtered electron tomography, *Appl. Phys. Lett.* 100 (2012) 101604.
- [26] X.Y. Zhong, J. Zhu, A.H. Zhang, S.C. Mou, Investigation of Electron structure in the ordered and disordered Ni_3Fe by electron energy loss spectroscopy, *Appl. Phys. Lett.* 89 (2006) 151912.
- [27] P.-L. Ho, C.-P. Yu, Q.Q. Zhang, K. Song, J.P. Buban, S.-Y. Choi, R.E. Dunin-Borkowski, J. Mayer, N.-H. Tai, J. Zhu, L. Jin, X.Y. Zhong, Effect of cation ratio and order on magnetic circular dichroism in the double perovskite $\text{Sr}_2\text{Fe}_{1-x}\text{Re}_x\text{O}_6$, *Ultramicroscopy* 193 (2018) 137–142.
- [28] B. Cui, P. Werner, T.P. Ma, X.Y. Zhong, Z.C. Wang, J.M. Taylor, Y.C. Zhuang, S.S.P. Parkin, Direct imaging of structural changes induced by ionic liquid gating leading to creation of three-dimensional meso-structures, *Nat. Commun.* 9 (2018) 3055.
- [29] L. Jin, C.L. Jia, I. Lindfors-Vrejoiu, X.Y. Zhong, H.C. Du, R.E. Dunin-Borkowski, Direct demonstration of a magnetic dead layer resulting from a-site cation inhomogeneity in a (La,Sr)MnO₃ epitaxial film system, *Adv. Mater. Interfaces* 3 (2016) 1600414.
- [30] J. Lin, X.Y. Zhong, C. Song, J. Ruzs, V. Kocovski, H.L. Xin, B. Cui, L.L. Han, R.Q. Lin, X.F. Chen, J. Zhu, Detection of magnetic circular dichroism in amorphous materials utilizing a single-crystalline overlayer, *Phys. Rev. Mater.* 1 (2017) 071404 (R).
- [31] S. Higashikozono, K. Ito, F. Takata, T. Gushi, K. Toko, T. Suemasu, Highly oriented epitaxial ($\alpha'' + \alpha'$)- Fe_{16}N_2 films on α -Fe(001) buffered MgAl_2O_4 (001) substrates and their magnetization, *J. Cryst. Growth* 468 (2017) 691–695.
- [32] J.M.D. Coey, The magnetization of bulk α' - Fe_{16}N_2 (invited), *J. Appl. Phys.* 76 (1994) 6632–6636.
- [33] M. Hegggen, M. Luysberg, K. Tillmann, FEI Titan 80-300 STEM, *J. Large-Scale Res. Facil.* 2 (2016) A42.
- [34] J. Ruzs, S. Muto, K. Tatsumi, New algorithm for efficient Bloch-waves calculations of orientation-sensitive ELNES, *Ultramicroscopy* 125 (2013) 81–88.
- [35] N. Ji, Y.M. Wu, J.-P. Wang, Epitaxial high saturation magnetization FeN thin films on Fe (001) seeded GaAs (001) single crystal wafer using facing target sputterings, *J. Appl. Phys.* 109 (2011) 07B767.
- [36] D.H. Pearson, C.C. Ahn, B. Fultz, White lines and d-electron occupancies for the 3d and 4d transition metals, *Phys. Rev. B* 47 (1993) 8471–8478.